Bioactive Materials 17 (2022) 289–299

Contents lists available at ScienceDirect

Bioactive Materials

journal homepage: www.keaipublishing.com/en/journals/bioactive-materials

Triple-synergistic MOF-nanozyme for efficient antibacterial treatment

Muxue Wang [b], Xi Zhou [b], Yunhong Li [a], Yuqing Dong [c], Jiashen Meng [d], Shuai Zhang [b], Linbo Xia [b], Zhaozhi He [b], Lei Ren [b], Zhiwei Chen [a,**], Xingcai Zhang [c,d,*]

[a] Department of Electronic Science, Fujian Provincial Key Laboratory of Plasma and Magnetic Resonance Research, School of Electronic Science and Engineering, Xiamen University, Xiamen, 361005, People's Republic of China
[b] The Higher Educational Key Laboratory for Biomedical Engineering of Fujian Province, Research Center of Biomedical Engineering of Xiamen, Department of Biomaterials, College of Materials, Xiamen University, Xiamen, 361005, People's Republic of China
[c] John A Paulson School of Engineering and Applied Sciences, Harvard University, Cambridge, MA, 02138, USA
[d] School of Engineering, Massachusetts Institute of Technology, Cambridge, MA, 02139, USA

ARTICLE INFO

Keywords:
Metal-organic frameworks
Nanozyme
Reactive oxygen species
Antibacterial
Zinc ion

ABSTRACT

The abuse of antibiotics makes bacterial infection an increasingly serious global health threat. Reactive oxygen species (ROS) are the ideal alternative antibacterial approach for quick and effective sterilization. Although various antibacterial strategies based on ROS have been developed, many of them are still limited by insufficient antibacterial efficiency. Here, we have developed an acid-enhanced dual-modal antibacterial strategy based on zeolitic imidazolate frameworks-8 (ZIF8) -derived nanozyme. ZIF8, which can release Zn^{2+}, is chosen as the carrier to integrate glucose oxidase (GOx) and gold nanoparticles (Au NPs) which can produce ROS via a cascade catalytic reaction. Thus, the bactericidal capability of ROS and Zn^{2+} have been integrated. More importantly, gluconic acid, a "by-product" of the catalytic reaction, can generate an acidic environment to promote both the ROS-producing and Zn^{2+}-releasing, enhancing the overall antibacterial performance further. This triple-synergistic strategy exhibits extraordinary bactericidal ability at a low dosage of 4 μg/mL (for *S. aureus*) and 8 μg/mL (for *E. coli*), which shows a great potential of MOF-derived nanozyme for efficient bacterial eradication and diverse biomedical applications.

1. Introduction

Bacterial infection, which may cause serious tissue damage and chronic non-healing wound, has become a serious global health threat [1]. The increasing risk of drug-resistant bacteria has limited the development of antibiotics dramatically [2]. Alternative strategies to achieve bacterial sterilization and prevent drug resistance should be encouraged. In recent years, strategies based on photo-thermal/photodynamic [3–5], cations [6,7], metallic ions [8–10], nanozymes [11–14], surface topographies [15], and antibacterial peptides/drugs [16,17] have been reported widely. Generally, single-modal antibacterial strategies have limited antibacterial effects or require high-dose usage [18]. Therefore, there is an urgent need for dual/multi-modal strategies for highly efficient antibacterial therapy and diverse biomedical applications [19].

The modes of toxicity when designed nanoparticles interact with a bacterium involve disruption of electron transport chains, cell membrane disruption, release of heavy metals, damage of proton efflux pumps, and generation of reactive oxygen species (ROS) [20]. Among them, ROS has been proved to be a rapid, effective, and broad-spectrum antibacterial and even anti-cancer strategy, and it is not inclined to promote drug-resistant bacteria [21–31]. Moreover, ROS is reactive with DNA and lipids of inactive bacteria, especially to the multidrug-resistant "superbugs" and the refractory biofilms, exhibiting an excellent antibacterial potential [32]. However, the direct introduction of high concentrated H_2O_2 will cause damage to normal tissues [33]. Furthermore, the relatively high pH (~6) in the bacterial biological systems limits the generation of ROS which usually requires an acidic environment with a pH of 3–4 [34,35]. Until now, several strategies have been suggested to address the inefficient generation of ROS

Peer review under responsibility of KeAi Communications Co., Ltd.
* Corresponding author. John A Paulson School of Engineering and Applied Sciences, Harvard University, Cambridge, MA, 02138, USA.
** Corresponding author. Department of Electronic Science, Fujian Provincial Key Laboratory of Plasma and Magnetic Resonance Research, School of Electronic Science and Engineering, Xiamen University, Xiamen 361005, People's Republic of China.
E-mail addresses: chenzhiwei@xmu.edu.cn (Z. Chen), xingcai@mit.edu (X. Zhang).

https://doi.org/10.1016/j.bioactmat.2022.01.036
Received 20 October 2021; Received in revised form 19 January 2022; Accepted 19 January 2022
Available online 1 February 2022

in an infected area. An efficient way is to design nanoplatforms with high catalytic activities. For instance, Mu [36] constructed bifunctionalized $NiCo_2O_4$–Au NPs with excellent oxidase and peroxidase catalytic activities, achieving an effective bacteria eradication at a relatively low concentrated H_2O_2. Alternatively, Liu [37] and Cheng [38] introduced glucose oxidase (GOx) to generate gluconic acid to create an environment with a lower pH value, increasing the production of ROS so as the antibacterial efficiency. Nonetheless, it still requires a high-dose usage to achieve effective bacterial eradication (100 μg/mL for 10^6 CFU/mL bacteria). Therefore, it remains a great challenge to develop a highly efficient antibacterial therapy and decrease the usage of antibacterial agents.

Ions, such as Ag^+, Cu^{2+}, and Zn^{2+}, is another effective way of bacterial killing due to their direct damage to the bacterial membrane and proteins [39–42]. Metal-organic frameworks (MOFs), consisting of metal ions and organic ligands, could act as the carrier for various substances, making it an ideal platform for antibacterial therapy [43–53]. Among them, zeolitic imidazolate frameworks-8 (ZIF8), consisting of transition-metal Zn and imidazolate linkers, could be degraded gradually and release abundant Zn^{2+} in an acid environment to make chemical damage to bacteria [54–56]. More importantly, the release of Zn^{2+} of ZIF8 exhibits a pH-dependent behavior which is a positive correlation with the antibacterial ability [57–58]. Thus, it is possible to develop an acid-enhanced dual-modal antibacterial therapy via integrating GOx and Au nanozyme (peroxidase-like) into ZIF8 (ZIF8/Au--GOx NPs) (Fig. 1a). On one hand, ZIF8 could act as the carrier to load GOx and Au which catalyze glucose into ROS through a cascade reaction to achieve bacterial killing. And the small cavity (~2.0 nm) of ZIF8 could act as the pathway for substrate diffusion to facilitate the interaction of reactants, pursuing higher catalytic efficacy [59–61]. On the other hand, the Zn^{2+} releasing from ZIF8 could also realize the antibacterial property. Moreover, gluconic acid, a by-product of the cascade reaction, could generate an acidic environment to promote the enzymatic catalysis and Zn^{2+}-releasing in turn, enhancing the overall bacterial eradication (Fig. 1b). Systematic antibacterial experiments have been carried out to illustrate that ZIF8/Au-GOx NPs (ZAG) NPs has a superior antibacterial property at even low concentrations (8 μg/mL for *E. coli* and 4 μg/mL for *S. aureus*). The wound healing observation proves the effective bacterial eradication *in vivo*, together with the biocompatibility. Hence, an acid-enhanced dual-modal strategy of ROS producing ability and Zn^{2+}-releasing performance has been integrated into ZAG NPs to develop a highly efficient antibacterial therapy, promoting the development of dual/multi-modal strategies in biochemical and biomedical fields.

2. Materials and methods

2.1. Materials

Zinc nitrate hexahydrate ($Zn(NO_3)_2$), chloroauric acid ($HAuCl_4$), sodium borohydride ($NaBH_4$), potassium dihydrogen phosphate (KH_2PO_4), and disodium phosphate (Na_2HPO_4) were purchased from Sinopharm Chemical Reagent Co., Ltd. Propidium iodide (PI), 4′,6-diamidino-2-phenylindole (DAPI), glucose oxidase, 3,3′,5,5′-tetramethylbenzidine (TMB), and LB Broth were purchased from BBI Life Sciences Corporation. 2-Methylimidazole (2-MI) was purchased from Yinuokai Technology Co., Ltd. β-D-glucose was purchased from Aladdin (Shanghai, China). And LB Broth agar medium was purchased from Dalian Meilunbio Do., Ltd. All other reagents were purchased from Xilong Science Co., Ltd.

2.2. Instrument and characteristics

X-ray diffraction (XRD) patterns were characterized using an X-ray powder diffractometer (Rigaku, SmartLab SE). UV-vis spectra were determined via UV-vis spectrophotometer (Shimadzu, UV-1750). Transmission electron microscopy (TEM) images were obtained by JEM-1400 (Jeol) at 100 kV. Elemental analysis was carried out by F200s (Talos). Scanning electron microscopy (SEM) images were obtained by SU-70 (Hitachi) at 5 kV. Hydrodynamic diameter and zeta potential were measured by dynamic light scattering (DLS) using the Malvern ZEN 3600. The release of Zn^{2+} ions was detected via an inductively coupled plasma optical emission spectrometer (ICP-OES, OPTIMA 2 × 00/5000). Thermal weight loss was evaluated by a simultaneous thermal analyzer (NETZSCH, STA 449F5). Reactive oxygen species were determined by electron spin resonance spectrometer (Bruker, EMX-10/12). Fluorescence images were observed and recorded by Leica DM 6000 B. Bacterial counting and Area calculating are obtained by NIH ImageJ Software. Agar blocks were cut into ultra-thin slices by Ultra-thin microtome (Leica Microsystems, Leica UC7).

2.3. Synthesis of ZIF8 NPs

2-methylimidazole (37.50 mmol) and $Zn(NO_3)_2{\cdot}6H_2O$ (7.50 mmol)

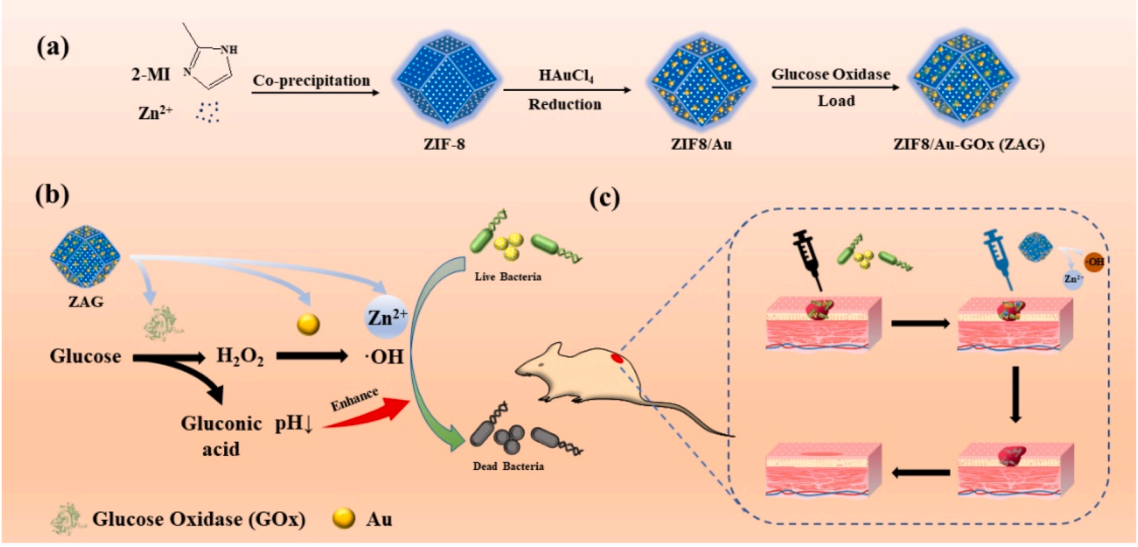

Fig. 1. (a) Illustration of the synthesis of ZIF8/Au-GOx NPs. (b) Reaction mechanism of the effective acid-enhanced dual-modal strategy for antibacterial treatment. (c) The ZIF8/Au-GOx NPs used for antibacterial therapy of mice.

were added to methanol (150 mL), respectively. The solutions were mixed and then stand at room temperature for 24 h. After centrifuging and washing with methanol three times and drying in a vacuum overnight, the ZIF8 powder was obtained.

2.4. Synthesis of ZIF8/Au NPs

50 mg ZIF8 powder was dispersed in 50 mL methanol and then ultrasonic for 20 min. Next, 750 μL of chloroauric acid methanol solution (20 mM) was added into the above uniformly dispersed ZIF8 solution for another 20-min of ultrasonication. Then, 3.75 mL $NaBH_4$ methanol solution (0.1 M) was added into the above mixture with vigorous stirring. During the stirring, the solution gradually turned purple. After 1 h, the resulting precipitate could be separated and obtained from the solution by centrifugation. After being washed several times with methanol and dried in a vacuum oven overnight, ZIF8/Au NPs could be acquired.

2.5. Synthesis of ZIF8/Au-GOx NPs

20 mg of the obtained ZIF8/Au NPs was dispersed into 20 mL ultrapure water under mild magnetic stirring. A total of 20 mg GOx in 20 mL ultra-pure water was then added into the above ZIF8/Au solution with mild stirring for another 2 h. Finally, ZAG NPs could be obtained by centrifugation.

2.6. Analysis of catalytic performance

The generation of ·OH was detected via a colorimetric reaction using a TMB probe and characterized by UV-Vis spectrophotometer and electron spin resonance (ESR) in which DMPO was used as the spin trap. In colorimetric reaction, a mixture containing 200 μg/mL ZAG NPs, 4 mM TMB, and 10 mM glucose was prepared, and the UV-Vis absorption spectra from 340 nm to 800 nm were recorded after the color of the mixture was changed. The reaction of ZIF8/Au, H_2O_2, and TMB was also investigated while the concentration of H_2O_2 is 100 μM. In ESR measurements, a mixture containing 200 μg/mL ZAG NPs, 50 mM DMPO, and 10 mM glucose was prepared, and the ESR signals were recorded immediately. The ·OH generated by ZIF8/Au with H_2O_2 was tested following the same procedure while the concentration of H_2O_2 is also 10 mM.

For the steady-state kinetic analysis, the PBS of various pH values (3.5, 4.5, 5.5, 6.5) containing TMB (3.2 mM), H_2O_2, and ZIF8/Au (200 μg/mL) were mixed and detected immediately via the UV-Vis spectrophotometer at 650 nm. When the pH value of the PBS was set as 4.5, H_2O_2 concentration was set as 12.5, 25, 100, and 200 mM separately. Equations used here are listed below.

$$A = kbc \tag{1}$$

$$\upsilon_0 = \frac{V_{max} \cdot [S]}{K_M + [S]} \tag{2}$$

$$\frac{1}{\upsilon_0} = \frac{K_M}{V_{max}} \cdot \frac{1}{[S]} + \frac{1}{V_{max}} \tag{3}$$

2.7. Evaluation of antibacterial performance

First, the minimal inhibition concentrations (MIC) of ZAG NPs with or without the addition of glucose were monitored. For the MIC of ZAG NPs co-incubation with *E. coli*, ZAG NPs at different concentrations (0, 1, 2, 4, 8, and 16 μg/mL) with 10 mM glucose were added to the same number of bacteria suspensions (10^6 CFU/mL dispersed in 25 g/L LB Broth solution). Then, the suspensions were incubated at 37 °C overnight. The concentration of the bacteria was measured by a microplate reader at 560 nm. And the bacterial suspensions were diluted 10^6 times and cultured on agar plates for 12 h to count the bacterial colonies. The agar plates were prepared by curing a PBS solution containing 0.04 g/mL LB Broth agar medium. As for the MIC of ZAG NPs co-incubation with *S. aureus*, the same method was used while the concentration of ZAG NPs changed into 0, 0.25, 0.5, 1, 2, and 4 μg/mL.

For the time-dependent optical density at 560 nm (OD_{560}) of various groups, 8 μg/mL nanoparticles for *E. coli* are applied. For the glucose (Glu) group and ZAG + Glu group, 10 mM glucose was added. The OD_{560} was recorded by a microplate reader several times. After 24 h' recording, the bacterial suspensions were diluted 10^7 times and cultured on agar plates for 12 h. The time-dependent optical density of *S. aureus* in different groups was conducted via the same method while the concentration of nanoparticles was set as 4 μg/mL.

The fluorescence microscopy images of bacteria treated with different samples were obtained by fluorescence test through DAPI/PI double staining [62]. The bacterial suspension (~10^8 CFU/mL) was mixed with the nanoparticles (ZIF8, ZIF8/Au, ZAG, ZAG + Glu) and incubated for 2 h. After that, the bacteria were obtained by centrifuging with sterile PBS 3 times. Then the above bacteria samples were incubated with a mixture of 1.5 μg/mL DAPI and 1.0 μg/mL PI at 37 °C for 15 min, followed by washing with sterile PBS 3 times and observed by fluorescence microscope.

To observe the morphologies of the bacteria, the suspensions of bacteria and nanoparticles were fixed with 2.5 wt% glutaraldehyde solution followed by dehydrating with gradient ethanol solutions (10, 30, 50, 70, 90, 100 wt%), and then detected by SEM. For TEM observation, after fixing with 2.5 wt% glutaraldehyde solution, the bacteria samples were embedded in agar and sliced before the observation.

2.8. In vivo animal experiments and histological analysis

The experimental mice (BALB/c, 4-6 weeks old) were purchased from Beijing Vital River Laboratories Animal Technology Co. Ltd.. All the animal experiments were carried out following the protocol set up by the Institutional Animal Care and Use Committee of Xiamen University. After anesthetized with 2% sodium pentobarbital, the bacterial infected wound model was established by nicking wound with a diameter of ≈7 mm on the back of every mouse, followed by deposition of *S. aureus* suspensions with a density of 10^8 CFU/mL. After 24 h, different treatments were carried out. One group was set as the blank control group and treated with PBS, while the other 5 groups were treated with 50 mM glucose, ZIF8 NPs (20 μg/mL), ZIF8/Au NPs (20 μg/mL), ZAG NPs (20 μg/mL) or ZAG NPs (20 μg/mL) with glucose (50 mM), respectively. The day of treatment was set as day 0. The bodyweight and wound sizes of mice in all groups were recorded every other day. The wound area was calculated via the ImageJ software. After 8 days of observation, the mice were sacrificed and the wounds were collected together with heart, liver, spleen, lung, and kidney for H&E analysis staining.

3. Results and discussion

3.1. Synthesis and characterization of ZIF8/Au-GOx

To prepare the ZIF8/Au-GOx (ZAG) NPs, ZIF8 NPs was first synthesized via the solvothermal method, which was then followed by the *in situ* reduction of $HAuCl_4$ to obtain the ZIF8/Au NPs. And ZAG NPs was finally obtained by the mixture of ZIF8/Au and GOx. Morphologies of the above nanoparticles were detected by transmission electron microscopy (TEM) and shown in Fig. 2a. For ZIF8, uniform hexagon morphologies are exhibited, which refers to the typical rhombic dodecahedral shape of ZIF8 nanocrystals. After the coating of Au NPs and GOx on ZIF8, it could be observed that Au NPs with diameters about 4 nm were homodispersed in ZIF8 NPs, and the morphologies of ZIF8/Au NPs remained the uniform hexagons. Besides, the decreased size of ZIF8 after integrating Au NPs and GOx could be attributed to the introduction of $HAuCl_4$ during the formation of Au NPs which caused a partial degradation of ZIF8 in the reaction. In Fig. 2b, the diffraction

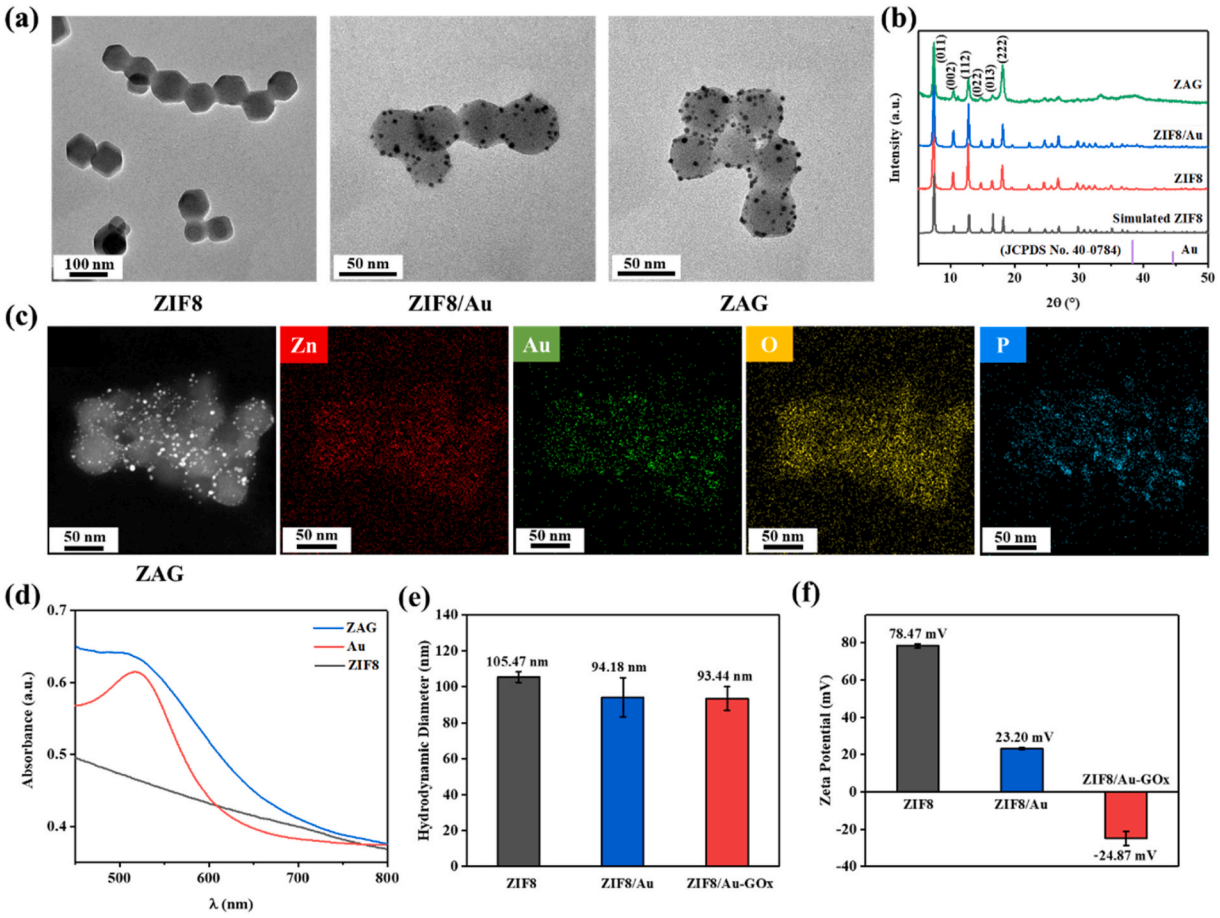

Fig. 2. (a) TEM images of ZIF8, ZIF8/Au, and ZIF8/Au-GOx NPs. (b) XRD pattern of ZIF8, ZIF8/Au, and ZIF8/Au-GOx NPs. (c) Dark-field image and the corresponding area-elemental mappings of ZIF8/Au-GOx NPs. (d) The UV-Vis absorption spectra of Au, ZIF8, and ZIF8/Au-GOx (ZAG) NPs. The hydrodynamic diameter (e) and zeta potential (f) of ZIF8, ZIF8/Au, and ZIF8/Au-GOx NPs.

peaks of ZIF8 are completely consistent with the simulation, referring to the successful synthesis of ZIF8 NPs. The unchanged XRD patterns between ZIF8, ZIF8/Au, and ZAG NPs reveal that the as-prepared ZIF8/Au NPs and ZIF8/Au-GOx NPs has the same crystal structure as ZIF8 NPs, while the particle size of Au NPs (~4 nm) is too small to be observed the planes in XRD spectra.

The element mapping images of ZAG NPs in Fig. 2c exhibit that the Au, O, and P are evenly distributed on ZAG NPs. Zn may belong to ZIF8 NPs, Au may belong to Au NPs, O and P may belong to GOx, which indicates that Au and GOx may decorate on ZIF8 NPs. The elements in ZAG NPs have been further confirmed by energy dispersive spectroscopy (EDS) in Fig. S1, which is consistent with the element mapping of ZAG NPs in Fig. 2c. And the characteristic absorption of UV-Vis spectrum at 520 nm of Au NPs and ZAG NPs illustrates the satisfactory integration of Au NPs within ZAG NPs further (Fig. 2d). Fig. 2e exhibits the hydrodynamic size of ZIF8, ZIF8/Au, and ZAG NPs, in which the size of ZIF8/Au and ZAG are larger than the diameters detected via TEM images (~50 nm) due to the reduced hydrophobicity of ZIF8 induced by Au NPs and GOx. The zeta potential of ZAG NPs is about -24.87 ± 3.78 mV because of the coating of negative GOx whose equipotential point is 4.9 (Fig. 2f). The zeta potential data of ZIF8, ZIF8/Au, and ZIF8/Au-GOx reveals the modification of each step which is also demonstrated by the surface area data (Fig. S2, Table S1) further. BCA protein and thermogravimetric test show that GOx exhibits a loading amount of 48.52% in ZAG NPs, while Au NPs of 26.34% (Fig. S3).

3.2. Catalytic performance and metal-ion-release capabilities

A cascade nanocatalyst was built based on the integration of Au NPs and GOx on ZIF8. Fig. 3a shows the design and the cascade reaction on ZAG NPs. First, GOx on ZAG NPs could effectively catalyze the glucose to produce H_2O_2 *in situ*. The generated H_2O_2 was then catalyzed by Au NPs to produce ROS. The catalytic activity of ZAG NPs was evaluated by a typical colorimetric method based on 3,3′,5,5′-tetramethylbenzidine (TMB) (Fig. 3b). In the presence of ZAG NPs and glucose, TMB could be oxidized into oxidized TMB (oxTMB) which exhibits characteristic absorbances at 370 and 652 nm. In the absence of ZAG NPs, negligible absorbance could be observed, indicating that the mixture of TMB and glucose did not induce any oxidation reaction. The above result indicates the cascade catalytic ability of ZAG NPs in the presence of glucose. Consistently, the characteristic absorbances appearing in the mixture of ZIF8/Au NPs, TMB and H_2O_2 prove the catalase catalytic ability of ZIF8/Au NPs (Fig. 3b). Characteristic signals of the 1:2:2:1 in the electron spin resonance test confirm that ROS produced via the cascade reaction here is the highly active and toxic hydroxyl radicals (·OH), guaranteeing the effective bactericidal performance (Fig. 3c). Fig. 3d exhibits the decrease of pH value during the catalytic reaction of ZAG NPs and glucose, referring to the produce of gluconic acid. As is shown, the gradually generated gluconic acid could lower the *in situ* pH value as low as around 4.5.

To confirm the promotion of decreased pH value to ROS-producing and Zn^{2+}-releasing, the pH-reliance catalytic behavior of ZIF8/Au NPs and the pH-reliance Zn^{2+} dissolution of ZAG NPs were evaluated. Since the catalytic reaction can oxidate TMB and lead to obvious absorption

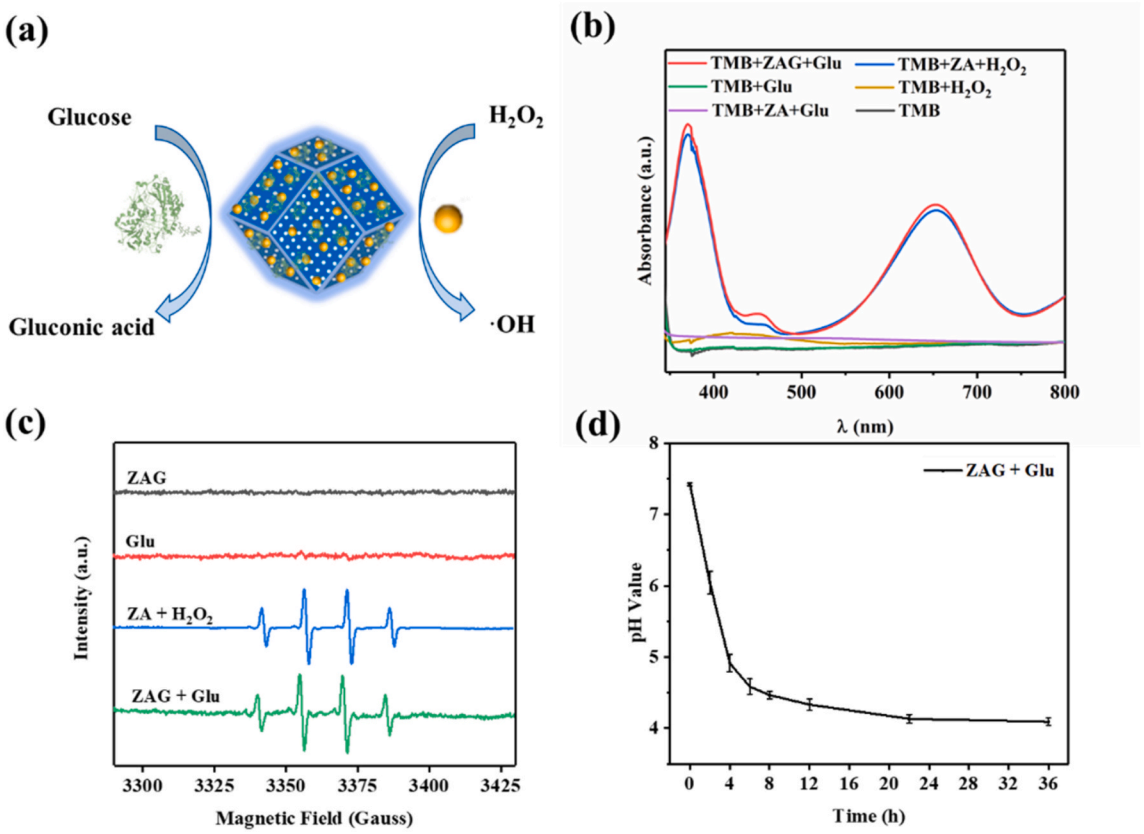

Fig. 3. (a) Schematic illustration of glucose reacting with ZIF8/Au-GOx. (b) UV-Vis absorption spectra of TMB catalyzed by blank, H_2O_2, glucose (Glu), ZIF8/Au (ZA), ZIF8/Au + H_2O_2, ZIF8/Au + glucose, ZAG, and ZAG + glucose. (c) ESR spectra of ZAG NPs, glucose, ZIF8/Au NPs with H_2O_2, and ZAG NPs with glucose using DMPO as the radical-scavenging nitrogen trap. (d) The change of pH value during the reaction of ZAG with glucose.

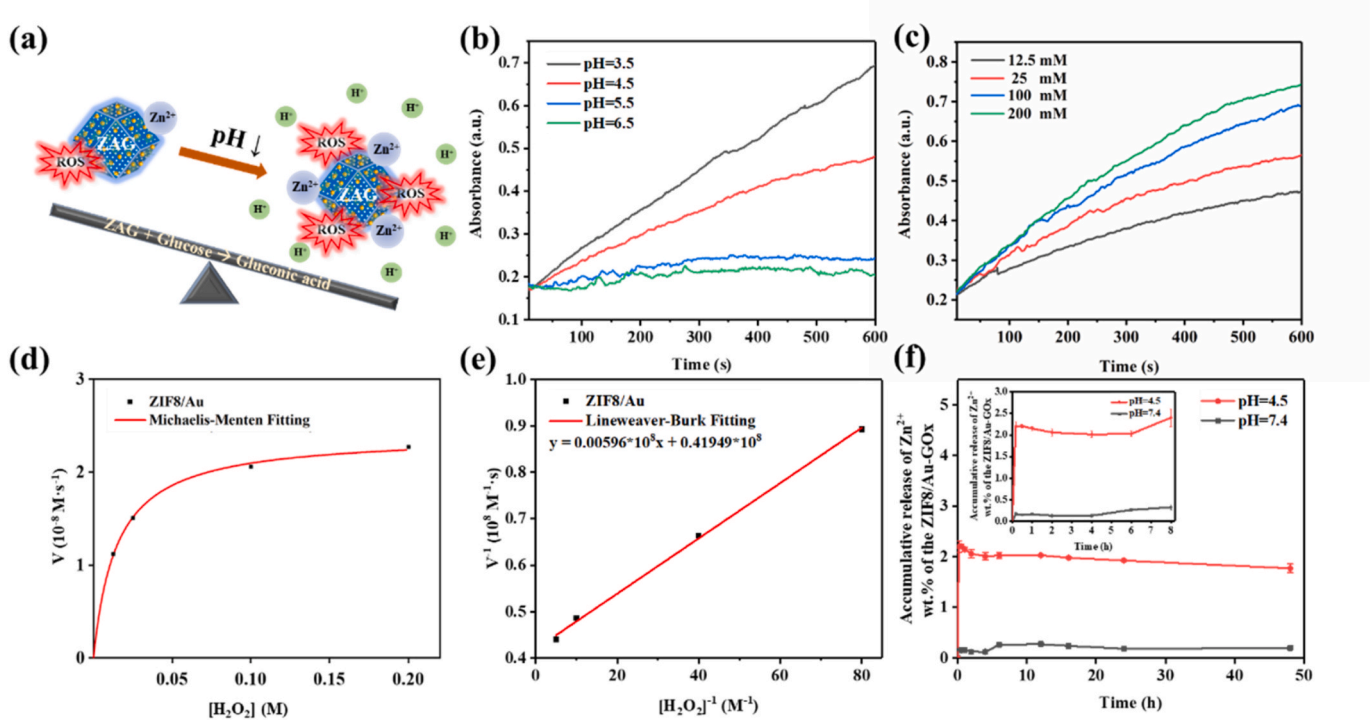

Fig. 4. (a) Schematic illustration of the acid-enhanced ROS-producing and Zn^{2+}-releasing performance of ZAG NPs. Absorbance of TMB chromogenic curves of ZIF8/Au NPs in the presence of H_2O_2 at (b) varied pH (3.5, 4.5, 5.5, and 6.5) and (c) varied H_2O_2 concentrations (12.5 mM, 25 mM, 100 mM, 200 mM). (d) Michaelis-Menten kinetics and (e) Lineweaver-Burk plotting of ZIF8/Au NPs. (f) The accumulative release of Zn^{2+} in ZAG in 48 h.

change, the time-dependent absorbance at 652 nm was monitored during the catalytic reaction to reveal the catalytic reaction rate at different pH values (Fig. 4b). As is shown, with the pH values decreased, the reaction rate increased. And when the pH value was 5 or 6, almost no obvious change of absorbance could be observed, which is consistent with the catalytic performance of Au NPs [63]. To determine the enhanced catalytic activity of ZIF8/Au NPs at the condition of gluconic acid generated in detail, the absorbance of ZIF8/Au NPs with different concentrations of H_2O_2 was monitored at a pH of 4.5 (Fig. 4c). K_M and V_{max} values of the catalytic reaction were calculated to be 14.21×10^{-3} M and 2.38×10^{-8} m/s according to Michaelis-Menten fitting (Fig. 4d) and Lineweaver-Burk fitting (Fig. 4e), guaranteeing the satisfactory catalytic efficacy. Therefore, the decrease of pH value induced by gluconic acid could enhance the catalytic of Au NPs to produce adequate ROS and ensure effective bactericidal performance.

To investigate the Zn^{2+}-release capability of ZAG NPs, the content of Zn^{2+} in PBS with different pH value (pH = 4.5 and pH = 7.4) were tested by inductively coupled plasma optical emission spectrometry (ICP-OES) at different time. Fig. 4f exhibits the cumulative Zn^{2+}-release capacity for ZAG within 48 h. In acidic condition (pH = 4.5), the release amount of Zn^{2+} increased significantly in the first 10 min and reached around 1.72 wt%, implying the potent antibacterial property of ZAG NPs in a very short time. For ZAG in the neutral condition, only 0.15 wt% Zn^{2+} can be released, which is approximately one-fifteenth of that in an acidic condition. Besides, we have also checked the morphology and XRD peaks of ZAG after Zn^{2+}-release in PBS (pH = 7.5) and in the acidic environment of pH = 4.5 in Fig. S4. As is shown, the collapsed structure of ZAG in the acidic environment and the relatively intact structure of it in PBS indicate the releasing of Zn^{2+} further. The missing diffraction peak at 2θ of about 7° in the acidic environment may be explained by the change of preferred orientation of ZAG after releasing Zn^{2+}. To sum up, the Zn^{2+}-release ability of ZAG NPs could be enhanced with the decrease of pH, which is coordinated with the pH-reliance catalytic performance of ZIF8/Au. Since the production of gluconic acid could lower the *in situ* pH value around 4.5 (Fig. 3d), both the ROS-producing and Zn^{2+}-releasing ability could be enhanced. As a result, ZAG NPs exhibited great potential for excellent bacterial eradication.

3.3. In vitro antibacterial performance

To evaluate the antibacterial ability of ZAG NPs, minimal inhibition concentrations (MIC) with or without the glucose to *E. coli* (Fig. 5a) or *S. aureus* (Fig. 5b) are measured. When the concentration of ZAG NPs reached 8 μg/mL, the absorbance (OD_{560}) of *E. coli* liquid medium containing ZAG NPs and glucose was the same as the blank group which only contain the liquid LB broth, indicating the complete growth inhibition to *E. coli*. Thus, the MIC value of ZAG NPs with glucose for *E. coli* could be determined as 8 μg/mL. And when the concentration of ZAG NPs was at the MIC value but without the addition of glucose, *E. coli* samples only exhibited an inhibition rate of 23.12%. Similarly, the MIC value of ZAG NPs with glucose for *S. aureus* is determined to be 4 μg/mL while the ZAG NPs caused an inhibition rate of 41.02% without glucose. The liquid mediums above were diluted and cultured on solid LB agar plates to evaluate the ability of bacterial eradication (Fig. S5). As is shown, no bacterial colony could be seen when the bacteria were cultured with glucose and ZAG NPs at the MIC value, illustrating the 100% bacterial eradication performance of ZAG NPs. These results manifest the excellent bactericidal ability of ZAG NPs for highly

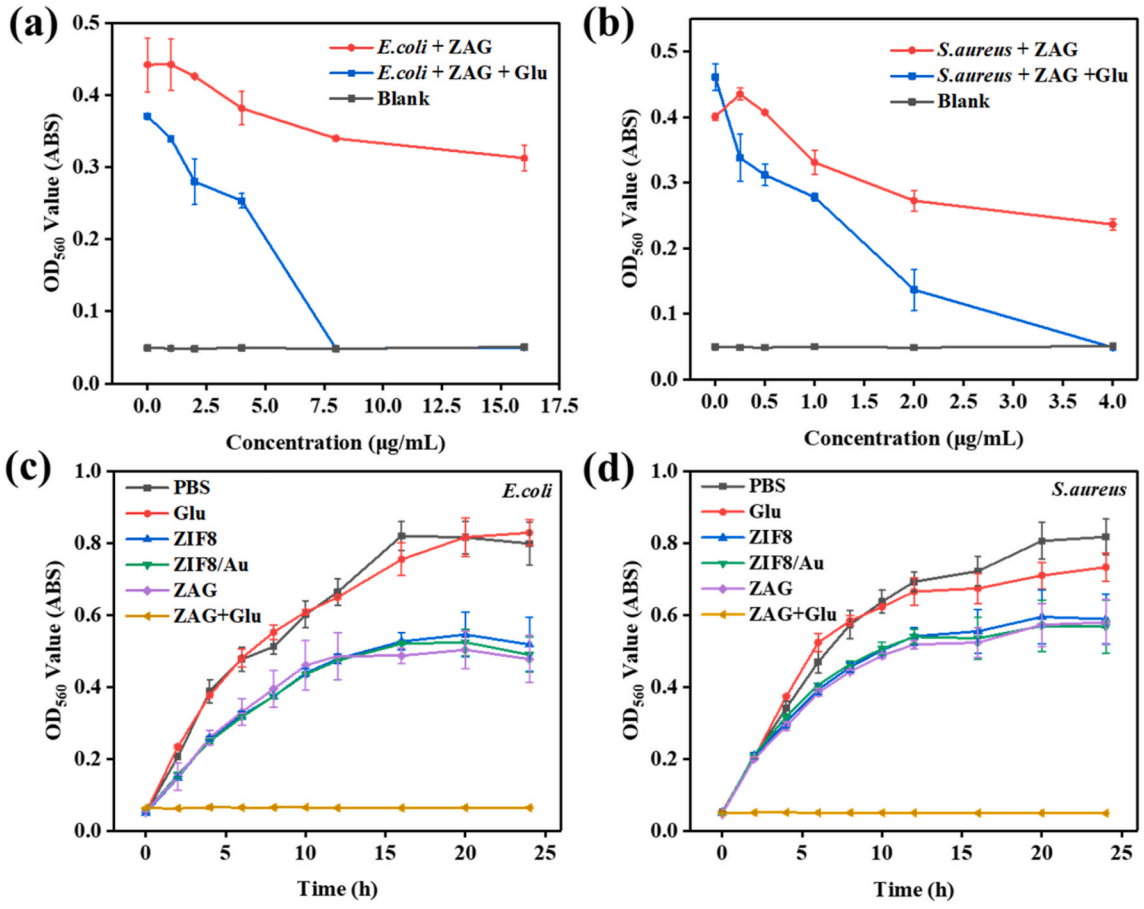

Fig. 5. The absorbance at 560 nm (OD_{560}) of (a) *E. coli* and (b) *S. aureus* liquid medium incubated with different concentrations of ZAG NPs with or without the addition of glucose (Glu). Time-dependent OD_{560} values of (c) *E. coli* and (d) *S. aureus* treated with PBS, glucose, ZIF8, ZIF8/Au, ZAG, and ZAG + glucose.

concentrated bacteria (10^6 CFU/mL) at a very low dosage of 8 μg/mL or 4 μg/mL, which could then reduce the usage of antibacterial agents effectively (Table S2).

Time-dependent OD_{560} value is monitored to investigate the influence of nanoparticles on the reproduction process of *E. coli* (Fig. 5c) and *S. aureus* (Fig. 5d). Besides, the solid agar plates of bacteria treated with different materials are present in Fig. 6. Optical density at 560 nm of the liquid medium is positive with the growth of bacteria, so OD_{560} values can reflect the reproduction of bacteria. For *E. coli*, the higher OD_{560} value or more colonies of bacteria treated with glucose than the PBS group could be explained for the energy supply effect of glucose to the *E. coli*. Compared with the PBS group whose OD_{560} value is obtained to be around 0.74 after 24 h incubation, lower OD_{560} values of ZIF8, ZIF8/Au, and ZAG group were observed due to the existence of ZIF8, suggesting the inhibition performance of Zn^{2+} to bacterial growth. *E. coli* co-incubation with both ZAG and glucose obtained the minimum OD_{560} value and none colony could be observed, and the inhibition effect of ZAG NPs appeared at the first 2 h, confirming the efficient bactericidal performance of ZAG NPs with glucose. Besides, as is shown in Fig. 6 (a), the physical mixture of Zn^{2+} + Au + GOx + Glu also exhibited an impressive bactericidal effect which could be explained by the Zn^{2+} and tandem catalysis induced by GOx and Au NPs. But with the introduction of ZIF-8 to immobilize and stabilize GOx and Au NPs, higher catalytic performance and the best bactericidal effect were achieved in group ZAG + Glu. Similar results were obtained on *S. aureus*, proving the universal antibacterial capability of ZAG NPs with glucose (Fig. 5d). All in all, ZIF8, ZIF8/Au, and ZAG NPs, which only possess the Zn^{2+}-releasing ability, show limited bacterial inhibition. ZAG NPs with acid-enhanced ROS-producing and Zn^{2+}-releasing ability, could achieve bacterial eradication efficiently in the presence of glucose, exhibiting outstanding bactericidal performance.

To further certify the direct damage of these nanoparticles to the bacterial membranes, fluorescence microscopy and scanning electron microscopy (SEM) images of bacteria treated in different conditions are detected (Fig. 7). For fluorescence observation, DAPI and PI were employed to stain the bacterium. Since the intact membrane is passable for DAPI with blue fluorescence but not for PI with red fluorescence, damages to bacterial membranes can be revealed by different fluorescence signals. And the morphologies of bacteria co-incubated with different materials are visualized via SEM. For the bacteria treated with PBS or glucose, none of dead bacteria could be observed and the bacteria show morphologies with complete membranes. For ZIF8, ZIF8/Au, and ZAG groups containing ZIF8 component, some dead bacteria could be detected and broken bacterial membranes appeared in SEM images, indicating that the released Zn^{2+} can cause damages to bacterial membranes and induce partial bacterial death which is consistent with the OD_{560} results. For ZAG with glucose group, almost no live bacteria could be observed, and all of the bacterial membranes were destroyed and stuck severely, indicating the severe damages caused by the produced ROS and released Zn^{2+}. Furthermore, detailed morphologies were obtained via the TEM images (Fig. 8). For bacteria treated with ZAG and glucose, broken or sunken bacterial membranes could be visualized clearly and the bacterium was stuck with each other due to the leaked cell contents. Concluding from the above investigation of the bacterial membrane, group of ZAG NPs with glucose caused the most severe damages and exhibited superior bactericidal performance. Therefore, we could conclude that the ZAG NPs, which possess Zn^{2+}-releasing and ROS-producing ability, could probably destroy bacterial membranes directly and lead to the leakage of cell contents at a low dosage, thus manifesting a great potential for bacterial eradication in the biological fields.

3.4. *In vivo* antibacterial performance

To evaluate the antibacterial efficiency of ZAG NPs in wound sterilization, we established the bacterial infection model and performed the treatment as shown in Fig. 9a. All mice were randomly divided into 6 groups, while one of which was treated with PBS and set as the blank

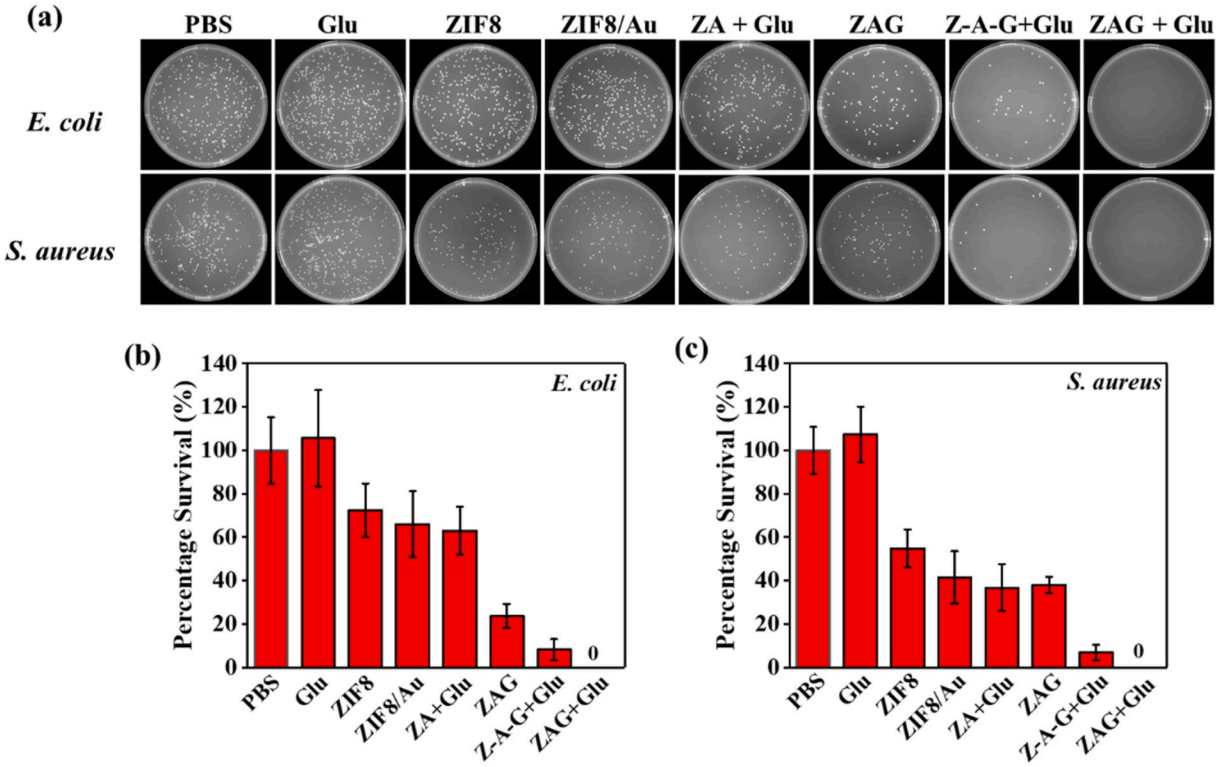

Fig. 6. (a) Solid agar plate photographs for *E. coli* and *S. aureus* treated with different materials (Z-A-G represents a physical mixture of Zn^{2+} + Au NPs + GOx), and (b, c) the corresponding statistical percentage survival.

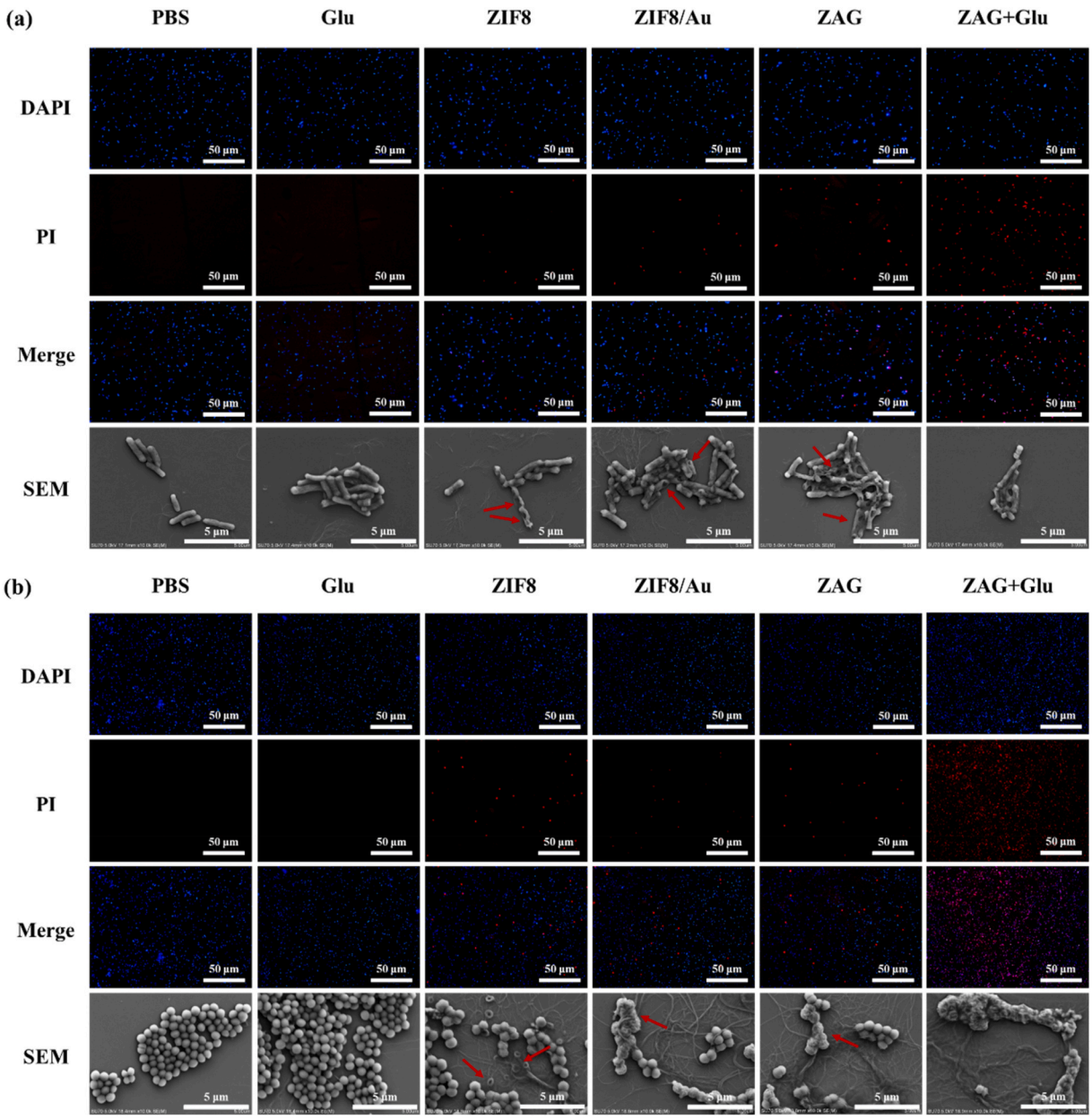

Fig. 7. Fluorescence microscopy images and SEM images for (a) *E. coli* and (b) *S. aureus* treated with PBS, glucose (Glu), ZIF8, ZIF8/Au, ZAG, and ZAG + glucose. (Red arrows indicate the broken bacteria structure).

control group. The other 5 groups were treated with glucose, ZIF8 NPs, ZIF8/Au NPs, ZAG NPs, or ZAG NPs with glucose respectively. Fig. 9b and c show the digital photos and relative area of wounds after the above different treatments. The quick sterilization in infected wound sites can reduce the inflammation so as to accelerate the process of wound regeneration. So, closure of the wound area could reveal the bacterial-killing effect in turn. For the glucose-treated group, only 40.20% of the relative wound area was closed during the whole treatment, which could be explained by the retarding effect of glucose towards the regeneration of vessels that provide nutrients for the regeneration process. Constant wound closure could be seen during the whole treatment period for mice in both PBS, ZIF8, ZIF8/Au, ZAG, and ZAG with glucose group, which presented 24.81%, 8.74%, 4.47%, 5.71%, and 0.13% of the relative wound area respectively at day 8. And the relatively faster closure of ZIF8, ZIF8/Au, and ZAG compared with PBS reveals the antibacterial ability of Zn^{2+} in ZIF8. It should be noticed that mice in ZAG with glucose groups exhibited an obvious wound closure compared to other groups on day 2, manifesting the excellent bactericidal performance.

To evaluate the wound healing process after bacterial eradication further, skin samples around the infected wound were collected for H&E staining to provide more reliable details (Fig. 10). For mice treated with glucose, incomplete skin tissues and several subcutaneous hemorrhages were observed which is consistent with the digital photos, indicating that the wound did not close completely. Mice in PBS group, ZIF8 group, ZIF8/Au group, and ZAG group exhibited similar tissue regeneration with arranged structure. Richly distributed capillary vessels which supply nutrients indicate the fast regeneration of skin tissues. Mice treated with both ZAG and glucose possessed well-formed skin structures and decreased capillary vessels, indicating complete regeneration of the wound site. Concluded from the above evaluation of antibacterial performance in wound sterilization, ZAG NPs with bacterial eradication capability could kill the bacterial effectively in the presence of glucose so as to accelerate the process of infected-wound healing.

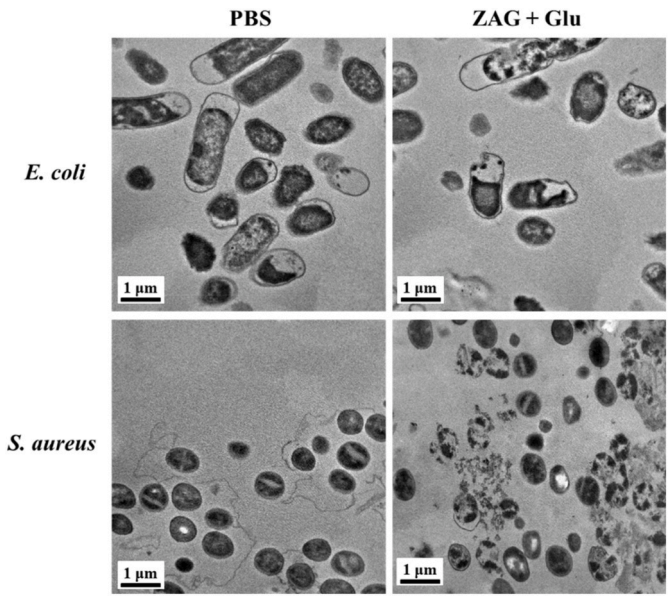

Fig. 8. TEM images for *E. coli* and *S. aureus* treated with PBS or ZIF8/Au-GOx (ZAG) + glucose (Glu).

Furthermore, during the whole therapeutic period, no significant weight abnormality appeared (Fig. 9d). And from histopathological images of major organs from the infected or treated mice in Fig. S6, no significant damage was observed after the therapy. All of the results demonstrate that ZAG NPs not only can achieve rapid and safe wound sterilization but also have good biocompatibility.

4. Conclusion

In summary, we have developed an acid-enhanced dual-modal bactericidal strategy via integrating ROS-producing ability and Zn^{2+}-releasing performance into ZAG NPs. First of all, the hydroxyl radicals and Zn^{2+} can cause damage to the bacterial membranes and induce the leakage of intracellular substances to eradicate bacteria. More importantly, gluconic acid generated during the catalytic reaction can lower the pH value of the infected area *in situ* around 4.5, which can improve both the ROS-producing and Zn^{2+}-releasing efficiency, resulting in an enhanced bacterial eradication ability. Systematical antibacterial experiments illustrate that the as-designed acid-enhanced dual-modal bactericidal strategy can achieve a 100% bactericidal ratio for *E. coli* and *S. aureus* (10^6 CFU/mL) at a very low dosage (8 μg/mL for *E. coli* and 4 μg/mL for *S. aureus*). *In vivo* assessment proves that the ZAG NPs can achieve rapid sterilization and promote the wound healing process on *S. aureus*-infected wounds. Considering the introduction of glucose in our system, this strategy may be a candidate for diabetes mellitus wounds. Overall, ZAG NPs with acid-enhanced dual antibacterial modal exhibit excellent bactericidal efficiency at a very low dosage, providing a novel strategy for multi-modal bacterial eradication in the biological field.

Declaration of competing interest

All authors declared no competing interests.

CRediT authorship contribution statement

Muxue Wang: Investigation, Methodology, Validation, Formal analysis, Writing – original draft. **Xi Zhou:** Conceptualization, Investigation, Resources, Writing – original draft, Writing – review & editing, Supervision. **Yunhong Li:** Investigation, Validation, Methodology.

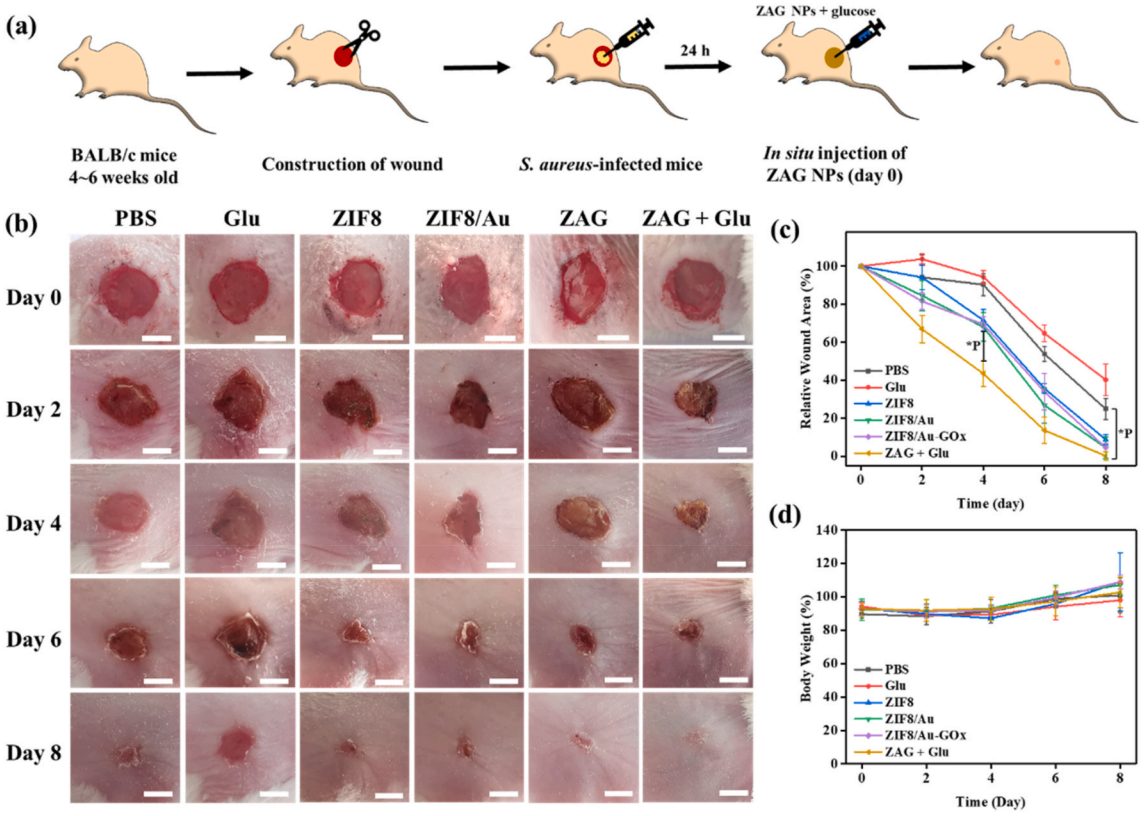

Fig. 9. (a) Schematic illustration of the *in vivo* antibacterial therapy process of ZIF8/Au-GOx (ZAG) NPs. Scale bar: 5 mm. (b) Photographs and (c) relative wound areas of the infected wound after different treatments on day 0, day 2, day 4, day 6, and day 8. (d) Bodyweight of mice during varied treatments.

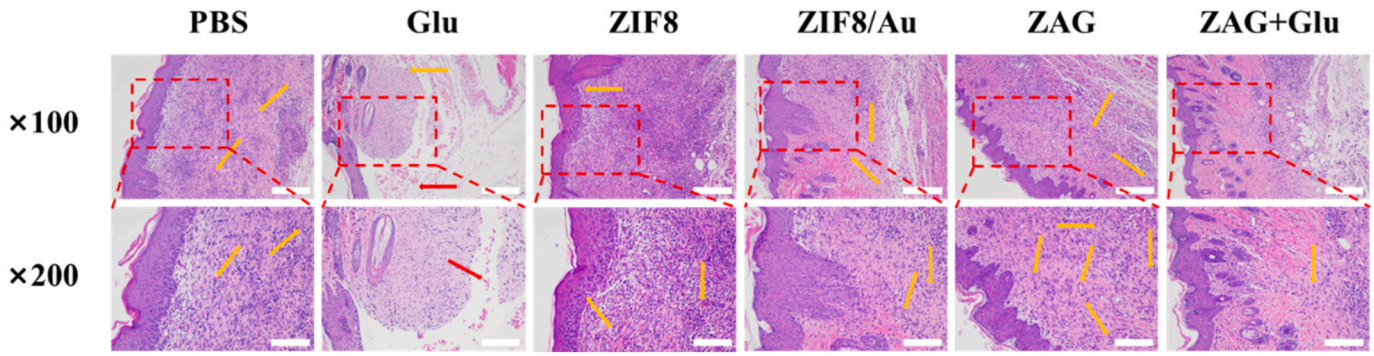

Fig. 10. Microscopic images of H&E-stained skin samples dissected from mice for histopathological analysis. Scale bar: × 100: 500 μm; × 200: 250 μm. (Red Arrows: subcutaneous hemorrhage; Orange arrows: capillary vessels).

Yuqing Dong: Investigation, Methodology. **Jiashen Meng:** Investigation, Methodology. **Shuai Zhang:** Validation, Methodology. **Linbo Xia:** Validation, Methodology. **Zhaozhi He:** Validation. **Lei Ren:** Resources, Methodology. **Zhiwei Chen:** Funding acquisition, Resources, Project administration, Supervision, Visualization, Writing – review & editing. **Xingcai Zhang:** Supervision, Writing – original draft, Writing – review & editing.

Declaration of competing interest

The authors declare that they have no conflict of interest.

Acknowledgments

This work was supported by the National Natural Science Foundation of China (U1904206, U190420008, 31870994), China Scholarship Council (201806315005 and 201703170071).

Appendix A. Supplementary data

Supplementary data to this article can be found online at https://doi.org/10.1016/j.bioactmat.2022.01.036.

References

[1] Z.W. Chen, Z.Z. Wang, J.S. Ren, X.G. Qu, Enzyme mimicry for combating bacteria and biofilms, Acc. Chem. Res. 51 (3) (2018) 789, https://doi.org/10.1021/acs.accounts.8b00011.

[2] I.B. Seiple, Z.Y. Zhang, P. Jakubec, A. Langlois-Mercier, P.M. Wright, D.T. Hog, K. Yabu, S.R. Allu, T. Fukuzaki, P.N. Carlsen, Y. Kitamura, X. Zhou, M.L. Condakes, F.T. Szczypinski, W.D. Green, A.G. Myers, A platform for the discovery of new macrolide antibiotics, Nature 533 (2016) 338–345, https://doi.org/10.1038/nature17967.

[3] J. Ouyang, X. Ji, X. Zhang, C. Feng, Z. Tang, N. Kong, A. Xie, J. Wang, X. Sui, L. Deng, Y. Liu, J.S. Kim, Y. Cao, W. Tao, In situ sprayed NIR-responsive, analgesic black phosphorus-based gel for diabetic ulcer treatment, Proc. Natl. Acad. Sci. U.S.A. 117 (46) (2020) 28667–28677, https://doi.org/10.1073/pnas.2016268117.

[4] Y.R. Wang, T. Wei, Y.C. Qu, Y. Zhou, Y.J. Zheng, C.B. Huang, Y.X. Zhang, Q. Yu, H. Chen Smart, Photothermally activated, antibacterial surfaces with thermally triggered bacteria-releasing properties, ACS Appl. Mater. Interfaces 12 (19) (2020) 21283–21291, https://doi.org/10.1021/acsami.9b17581.

[5] J. Li, S. Song, J. Meng, L. Tian, X. Liu, Y. Zheng, Z. Li, K.W.K. Yeung, Z. Cui, Y. Liang, S. Zhu, X. Zhang, S. Wu, 2D MOF periodontitis photodynamic ion therapy, J. Am. Chem. Soc. (2021), https://doi.org/10.1021/jacs.1c07875.

[6] X. Huang, L. Tian, Z.Y. Wang, J.Q. Zhang, Y.S. Chan, S.H. Cheng, X. Yao, Bioinspired robust all-aqueous droplet via diffusion-controlled interfacial coacervation, Adv. Funct. Mater. 30 (49) (2020) 2004166, https://doi.org/10.1002/adfm.202004166.

[7] S. Chen, S. Zhang, M. Galluzzi, F. Li, X. Zhang, X. Yang, X. Liu, X. Cai, X. Zhu, B. Du, J. Li, P. Huang, Insight into multifunctional polyester fabrics finished by one-step eco-friendly strategy, Chem. Eng. J. 358 (2019) 634–642, https://doi.org/10.1016/j.cej.2018.10.070.

[8] S. Wang, Z. Shen, Z. Shen, Y. Dong, Y. Li, Y. Cao, Y. Zhang, S. Guo, J. Shuai, Y. Yang, C. Lin, M. Guo, X. Chen, X. Zhang, Q. Huang, Machine-learning micropattern manufacturing, Nano Today 38 (2021) 101152, https://doi.org/10.1016/j.nantod.2021.101152.

[9] M.J. Liang, M.Y. Zhang, S.S. Yu, Q. Wu, K. Ma, Y.Y. Chen, X.Q. Liu, C.S. Li, F. Wang, Silver-laden black phosphorus nanosheets for an efficient in vivo antimicrobial application, Small 16 (13) (2020) 1905938, https://doi.org/10.1002/smll.201905938.

[10] Y. Li, Y. Dong, Y. Yang, P. Yu, Y. Zhang, J. Hu, T. Li, X. Zhang, X. Liu, Q. Xu, Q. Huang, C. Lin, Rational design of silver gradient for studying size effect of silver nanoparticles on contact killing, ACS Biomater. Sci. Eng. 5 (2) (2019) 425–431, https://doi.org/10.1021/acsbiomaterials.8b01282.

[11] L.W. Wang, F.N. Gao, A.Z. Wang, X.Y. Chen, H. Li, X. Zhang, H. Zheng, R. Ji, B. Li, X. Yu, J. Liu, Z.J. Gu, F.L. Chen, C.Y. Chen, Defect-rich adhesive molybdenum disulfide/rGO vertical heterostructures with enhanced nanozyme activity for smart bacterial killing application, Adv. Mater. 32 (48) (2020) 2005423, https://doi.org/10.1002/adma.202005423.

[12] F. Cao, L. Zhang, H. Wang, Y. You, Y. Wang, N. Gao, J. Ren, X. Qu, Defect-rich adhesive nanozymes as efficient antibiotics for enhanced bacterial inhibition, Angew. Chem. Int. Ed. 58 (45) (2019) 16236–16242, https://doi.org/10.1002/anie.201908289.

[13] B.L. Xu, H. Wang, W.W. Wang, L.Z. Gao, S.S. Li, X.T. Pan, H.Y. Wang, H.L. Yang, X. Q. Meng, Q.W. Wu, L.R. Zheng, S.M. Chen, X.H. Shi, K.L. Fan, X.Y. Yan, H.Y. Liu, A single-atom nanozyme for wound disinfection applications, Chem. Int. Ed. 58 (15) (2019) 4911–4916, https://doi.org/10.1002/anie.201813994.

[14] Z.W. Liu, F.M. Wang, J.S. Ren, X.G. Qu, A series of MOF/Ce-based nanozymes with dual enzyme-like activity disrupting biofilms and hindering recolonization of bacteria, Biomaterials 208 (2019) 21–31, https://doi.org/10.1016/j.biomaterials.2019.04.007.

[15] T.L. Shi, X. Hou, S.Q. Guo, L. Zhang, C.H. Wei, T. Peng, X.G. Hu, Nanohole-boosted electron transport between nanomaterials and bacteria as a concept for nano-bio interactions, Nat. Commun. 12 (1) (2021) 493, https://doi.org/10.1038/s41467-020-20547-9.

[16] Y. Fan, X.D. Li, P.P. He, X.X. Hu, K. Zhang, J.Q. Fan, P.P. Yang, H.Y. Zheng, W. Tian, Z.M. Chen, L. Ji, H. Wang, L. Wang, A biomimetic peptide recognizes and traps bacteria in vivo as human defensin-6, Sci. Adv. 6 (19) (2020), https://doi.org/10.1126/sciadv.aaz4767 eaaz4767.

[17] R. Huang, M. Hu, W. Liang, J. Zheng, Y. Du, Y. Lin, H. Wang, W. Guo, Z. Zeng, C. Li, M. Li, H. Wang, X. Zhang, One-step preparation of green fabric for continuous antibacterial applications, Engineering 7 (3) (2021) 326–333, https://doi.org/10.1016/j.eng.2020.08.022.

[18] Y. Yang, X.Z. Wu, C. He, J.B. Huang, S.Q. Yin, M. Zhou, L. Ma, W.F. Zhao, L. Qiu, Metal-organic framework/Ag-based hybrid nanoagents for rapid and synergistic bacterial eradication, ACS Appl. Mater. Interfaces 12 (12) (2020) 13698–13708, https://doi.org/10.1021/acsami.0c01666.

[19] Y. Wang, Y.N. Yang, Y.R. Shi, H. Song, C.Z. Yu, Antibiotic-free antibacterial strategies enabled by nanomaterials: progress and perspectives, Adv. Mater. 32 (18) (2020) 1904106, https://doi.org/10.1002/adma.201904106.

[20] L. Jin, X. Guo, D. Gao, C. Wu, B. Hu, G. Tan, N. Du, X. Cai, Z. Yang, X. Zhang, NIR-responsive MXene nanobelts for wound healing, NPG Asia Mater. 13 (1) (2021) 24, https://doi.org/10.1038/s41427-021-00289-w.

[21] Q. Jiang, E. Fangjie, J.X. Tian, J.T. Yang, J.Y. Zhang, Y.Q. Cheng, Light-excited antibiotics for potentiating bacterial killing via reactive oxygen species generation, ACS Appl. Mater. Interfaces 12 (14) (2020) 16150–16158, https://doi.org/10.1021/acsami.0c02647.

[22] N. Kong, H. Zhang, C. Feng, C. Liu, Y. Xiao, X. Zhang, L. Mei, J.S. Kim, W. Tao, X. Ji, Arsenene-mediated multiple independently targeted reactive oxygen species burst for cancer therapy, Nat. Commun. 12 (1) (2021) 4777, https://doi.org/10.1038/s41467-021-24961-5.

[23] X. Ji, L. Ge, C. Liu, Z. Tang, Y. Xiao, Z. Lei, W. Gao, S. Blake, D. De, X. Zeng, N. Kong, X. Zhang, W. Tao, Capturing functional two-dimensional nanosheets from sandwich-structure vermiculite for cancer theranostics, Nat. Commun. 12 (1) (2021) 1124, https://doi.org/10.1038/s41467-021-21436-5.

[24] C. Liu, S. Sun, Q. Feng, Y. Wu, N. Kong, Z. Yu, J. Yao, X. Zhang, W. Chen, Z. Tang, Y. Xiao, X. Huang, A. Lv, Y. Cao, A. Wu, T. Xie, W. Tao, Arsenene nanodots with selective killing effects and their low-dose combination with ß-elemene for cancer therapy, Adv. Mater. 33 (37) (2021), e2102054, https://doi.org/10.1002/adma.202102054.

[25] W.Y. Kim, M. Won, S. Koo, X. Zhang, J.S. Kim, Mitochondrial H_2S_n-mediated anti-inflammatory theranostics, Nano-Micro Lett. 13 (2021) 168, https://doi.org/10.1007/s40820-021-00689-1.

[26] D. Wei, Y. Yu, X. Zhang, Y. Wang, H. Chen, Y. Zhao, F. Wang, G. Rong, W. Wang, X. Kang, J. Cai, Z. Wang, J. Yin, M. Hanif, Y. Sun, G. Zha, L. Li, G. Nie, H. Xiao, Breaking down the intracellular redox balance with diselenium nanoparticles for maximizing chemotherapy efficacyon patient-derived xenograft models, ACS Nano 14 (12) (2020) 16984–16996, https://doi.org/10.1021/acsnano.0c06190.

[27] D. Gao, T. Chen, Y. Han, S. Chen, Y. Wang, X. Guo, H. Wang, X. Chen, M. Guo, Y. S. Zhang, G. Hong, X. Zhang, Z. Tian, Z. Yang, Targeting hypoxic tumors with hybrid nanobullets for oxygen-independent synergistic photothermal-thermodynamic therapy, Nano-Micro Lett. 13 (1) (2021) 99, https://doi.org/10.1007/s40820-021-00616-4.

[28] W.C. Liu, Y. Pan, Y.T. Zhong, B.H. Li, Q.J. Ding, H.J. Xu, Y.Z. Qiu, F. Ren, B. Li, M. Muddassir, J.Q. Liu, A multifunctional aminated UIO-67 metal-organic framework for enhancing antitumor cytotoxicity through bimodal drug delivery, Chem. Eng. J. 412 (2021) 127899, https://doi.org/10.1016/j.cej.2020.127899.

[29] W.C. Liu, Q.W. Yan, C. Xia, X.X. Wang, A. Kumar, Y. Wang, Y.W. Liu, Y. Pan, J. Q. Liu, Recent advances in cell membrane coated metal–organic frameworks (MOFs) for tumor therapy, J. Mater. Chem. B 9 (22) (2021) 4459–4474, https://doi.org/10.1039/d1tb00453k.

[30] G.Z. Tan, Y.T. Zhong, L.L. Yang, Y.D. Jiang, J.Q. Liu, F. Ren, A multifunctional MOF-based nanohybrid as injectable implant platform for drug synergistic oral cancer therapy, Chem. Eng. J. 390 (2020) 124446, https://doi.org/10.1016/j.cej.2020.124446.

[31] Y.Y. Zhong, X.S. Li, J.H. Chen, X.X. Wang, L.T. Wei, L.Q. Fang, A. Kumar, S. Z. Zhuang, J.Q. Liu, Recent advances in MOF-based nanoplatforms generating reactive species for chemodynamic therapy, Dalton Trans. 49 (32) (2020) 11045–11058, https://doi.org/10.1039/d0dt01882a.

[32] M.J. Liang, Y.B. Wang, K. Ma, S.S. Yu, Y.Y. Chen, Z. Deng, Y. Liu, F. Wang, Engineering inorganic nanoflares with elaborate enzymatic specificity and efficiency for versatile biofilm eradication, Small 16 (41) (2020) 2002348, https://doi.org/10.1002/smll.202002348.

[33] Z.Z. Wang, K. Dong, Z. Liu, Y. Zhang, Z.W. Chen, H.J. Sun, J.S. Ren, X.G. Qu, Activation of biologically relevant levels of reactive oxygen species by Au/g-C3N4 hybrid nanozyme for bacteria killing and wound disinfection, Biomaterials 113 (2017) 145–157, https://doi.org/10.1016/j.biomaterials.2016.10.041.

[34] X.D. Wang, R.J. Meier, O.S. Wolfbeis, Fluorescent pH-sensitive nanoparticles in an agarose matrix for imaging of bacterial growth and metabolism, Angew. Chem. Int. Ed. 52 (1) (2013) 406–409, https://doi.org/10.1002/anie.201205715.

[35] X.L. Xie, T.C. Sun, J.Z. Xue, Z.H. Miao, X. Yan, W.W. Fang, Q. Li, R.P. Tang, Y. Lu, L.X. Tang, Z.B. Zha, T. He, Ag nanoparticles cluster with pH-triggered reassembly in targeting antimicrobial applications, Adv. Funct. Mater. 30 (17) (2020) 2000511, https://doi.org/10.1002/adfm.202000511.

[36] Q.Z. Mu, Y.F. Sun, A.Y. Guo, X.Y. Xu, B.P. Qin, A.J. Cai, A bifunctionalized $NiCo_2O_4$-Au composite: intrinsic peroxidase and oxidase catalytic activities for killing bacteria and disinfecting wound, J. Hazard Mater. 402 (2021) 123939, https://doi.org/10.1016/j.hazmat.2020.123939.

[37] X.P. Liu, Z.Q. Yan, Y. Zhang, Z.W. Liu, Y.H. Sun, J.S. Ren, X.G. Qu, Two-dimensional metal-organic framework/enzyme hybrid nanocatalyst as a benign and self-activated cascade reagent for in vivo wound healing, ACS Nano 13 (5) (2019) 5222–5230, https://doi.org/10.1021/acsnano.8b09501.

[38] X.Q. Cheng, S. Zhang, H.H. Liu, H.M. Chen, J.H. Zhou, Z.W. Chen, X. Zhou, Z. X. Xie, Q. Kuang, L.S. Zheng, Biomimetic metal-organic framework composite-mediated cascade catalysis for synergistic bacteria killing, ACS Appl. Mater. Interfaces 12 (30) (2020) 36996–37005, https://doi.org/10.1021/acsami.0c12159.

[39] F.Q. Han, S.P. Lv, Z.R. Li, L. Jin, B.B. Fan, J.J. Zhang, R. Zhang, X.C. Zhang, L. Han, J.G. Li, Triple-synergistic 2D material-based dual-delivery antibiotic platform, NPG Asia Mater. 12 (1) (2020) 15, https://doi.org/10.1038/s41427-020-0195-x.

[40] Y. Du, Z.K. Huang, S.Y. Wu, K.R. Xiong, X.C. Zhang, B.N. Zheng, R. Nadimicherla, R.W. Fu, D.C. Wu, Preparation of versatile yolk-shell nanoparticles with a precious metal yolk and a microporous polymer shell for high-performance catalysts and antibacterial agents, Polymer 137 (2018) 195–200, https://doi.org/10.1016/j.polymer.2017.12.069.

[41] C.H. Dong, W. Feng, W.W. Xu, L.D. Yu, H. Xiang, Y. Chen, J.Q. Zhou, The coppery age: copper (Cu)-Involved nanotheranostics, Adv. Sci. 7 (21) (2020), https://doi.org/10.1002/advs.202001549, 2001549.

[42] M.J. Liang, M.Y. Zhang, S.S. Yu, Q. Wu, K. Ma, Y.Y. Chen, X.Q. Liu, C.S. Li, F. Wang, Silver-laden black phosphorus nanosheets for an efficient in vivo antimicrobial application, Small 16 (13) (2020) 1905938, https://doi.org/10.1002/smll.201905938.

[43] J. Wu, F. Xu, S. Li, P. Ma, X. Zhang, Q. Liu, R. Fu, D. Wu, Porous polymers as multifunctional material platforms toward task-specific applications, Adv. Mater. 31 (4) (2019) 1802922, https://doi.org/10.1002/adma.201802922.

[44] J. Meng, Q. He, L. Xu, X. Zhang, F. Liu, X. Wang, Q. Li, X. Xu, G. Zhang, C. Niu, A novel dendrite-free Mn^{2+}/Zn^{2+} hybrid battery with 2.3 V voltage window and 11000-cycle lifespan, Adv. Energy Mater. 9 (29) (2019) 1802695, https://doi.org/10.1002/aenm.201901469.

[45] J. Meng, J. Li, J. Liu, X. Zhang, G. Jiang, L. Ma, Z.-Y. Hu, S. Xi, Y. Zhao, M. Yan, Universal approach to fabricating graphene-supported single-atom catalysts from doped ZnO solid solutions, ACS Cent. Sci. 6 (2020) 1431–1440, https://doi.org/10.1021/acscentsci.0c00458.

[46] J. Meng, Z. Liu, X. Liu, W. Yang, L. Wang, Y. Li, Y.-C. Cao, X. Zhang, L. Mai, Scalable fabrication and active site identification of MOF shell-derived nitrogen-doped carbon hollow frameworks for oxygen reduction, J. Mater. Sci. Technol. 66 (2021) 186–192, https://doi.org/10.1016/j.jmst.2020.07.007.

[47] B. Zheng, X. Lin, X. Zhang, D. Wu, K. Matyjaszewski, Emerging functional porous polymeric and carbonaceous materials for environmental treatment and energy storage, Adv. Funct. Mater. 30 (41) (2020) 1907006, https://doi.org/10.1002/adfm.201907006.

[48] Q.Q. Wang, X.P. Zhang, L. Huang, Z.Q. Zhang, S.J. Dong, GOx@ZIF-8(NiPd) nanoflower: an artificial enzyme system for tandem catalysis, Angew. Chem. Int. Ed. 56 (50) (2017) 16082–16085, https://doi.org/10.1002/anie.201710418.

[49] J.T. Yu, Z.X. Wei, Q. Li, F.Y. Wan, Z.C. Chao, X.D. Zhang, L. Lin, H. Meng, L.L. Tian, Advanced cancer starvation therapy by simultaneous deprivation of lactate and glucose using a MOF nanoplatform, Adv. Sci. 8 (19) (2021) 2101467, https://doi.org/10.1002/advs.202101467.

[50] H. Peng, X. Zhang, P. Yang, N. Feng, W. Yang, J. Tang, Defect self-assembly of metal-organic framework triggers ferroptosis to overcome resistance, Bioact. Mater. (2021), https://doi.org/10.1016/j.bioactmat.2021.12.018.

[51] L.Y. Chen, R. Luque, Y.W. Li, Controllable design of tunable nanostructures inside metal-organic frameworks, Chem. Soc. Rev. 46 (15) (2017) 4614–4630, https://doi.org/10.1039/c6cs00537c.

[52] L.Y. Chen, Q. Xu, Metal-organic framework composites for catalysis, Matter-US 1 (1) (2019) 57–89, https://doi.org/10.1016/j.matt.2019.05.018.

[53] X.M. Liu, Q.Q. Deng, L. Zhang, Y.J. Sang, K. Dong, J.S. Ren, X.G. Qu, Elimination of macrophage-entrapped antibiotic-resistant bacteria by a targeted metal-organic framework-based nanoplatform, Chem. Commun. 57 (23) (2021) 2903–2906, https://doi.org/10.1039/d0cc08340b.

[54] Y. Yang, X.Z. Wu, C. He, J.B. Huang, S.Q. Yin, M. Zhou, L. Ma, W.F. Zhao, L. Qiu, Metal-organic framework/Ag-based hybrid nanoagents for rapid and synergistic bacterial eradication, ACS Appl. Mater. Interfaces 12 (12) (2020) 13698–13708, https://doi.org/10.1021/acsami.0c01666.

[55] F.Y. Shao, Y.F. Wu, Z.Y. Tian, S.Q. Liu, Biomimetic nanoreactor for targeted cancer starvation therapy and cascade amplificated chemotherapy, Biomaterials 274 (2021) 120869, https://doi.org/10.1016/j.biomaterials.2021.120869.

[56] S. Yao, J.J. Chi, Y.T. Wang, Y.J. Zhao, Y. Luo, Y.A. Wang, Zn-MOF encapsulated antibacterial and degradable microneedles array for promoting wound healing, Adv. Healthc. Mater. 10 (12) (2021) 2100056, https://doi.org/10.1002/adhm.202100056.

[57] Z.Y. Song, Y. Wu, Q. Cao, H.J. Wang, X.R. Wang, H.Y. Han, pH-Responsive, light-triggered on-demand antibiotic release from functional metal-organic framework for bacterial infection combination therapy, Adv. Funct. Mater. 28 (23) (2018) 1800011, https://doi.org/10.1002/adfm.201800011.

[58] A. Sirelkhatim, S. Mahmud, A. Seeni, N.H.M. Kaus, L.C. Ann, S.K.M. Bakhori, H. Hasan, D. Mohamad, Review on zinc oxide nanoparticles: antibacterial activity and toxicity mechanism, Nano-Micro Lett. 7 (3) (2015) 219–242, https://doi.org/10.1007/s40820-015-0040-x.

[59] X. Zhou, W. Zhao, M.X. Wang, S. Zhang, Y.H. Li, W.X. Hu, L. Ren, S.L. Luo, Z. W. Chen, Dual-modal therapeutic role of the lactate oxidase-embedded hierarchical porous zeolitic imidazolate framework as a nanocatalyst for effective tumor SuppressionACS, Appl. Mater. Interfaces. 12 (29) (2021) 32278–32288, https://doi.org/10.1021/acsami.0c05783.

[60] X.C. Huang, Y.Y. Lin, J.P. Lin, J.P. Zhang, X.M. Chen, Ligand-directed strategy for zeolite-type metal-organic frameworks: zinc (II) imidazolates with unusual zeolitic topologies, Angew. Chem. Int. Ed. 45 (10) (2006) 1557–1559, https://doi.org/10.1002/anie.200503778.

[61] Y.C. Luo, K.L. Chu, J.Y. Shi, D.J. Wu, X.D. Wang, M. Mayor, C.Y. Su, Heterogenization of photochemical molecular devices: embedding a metal-organic cage into a ZIF-8-derived matrix to promote proton and electron transfer, J. Am. Chem. Soc. 141 (33) (2019) 13057–13065, https://doi.org/10.1021/jacs.9b03981.

[62] F. Wei, X.Y. Cui, Z. Wang, C.C. Dong, J.D. Li, X.J. Han, Recoverable peroxidase-like Fe_3O_4@MoS_2-Ag nanozyme with enhanced antibacterial ability, Chem. Eng. J. 408 (2021) 127240.

[63] Y.G. Zhang, S. Li, H.L. Liu, W. Long, X.D. Zhang, Enzyme-like properties of gold clusters for biomedical application, Front. Chem. 8 (2020) 219, https://doi.org/10.3389/fchem.2020.00219.